

# Continued Development of a Planetary Imaging Fourier Transform Spectrometer (PIFITS)

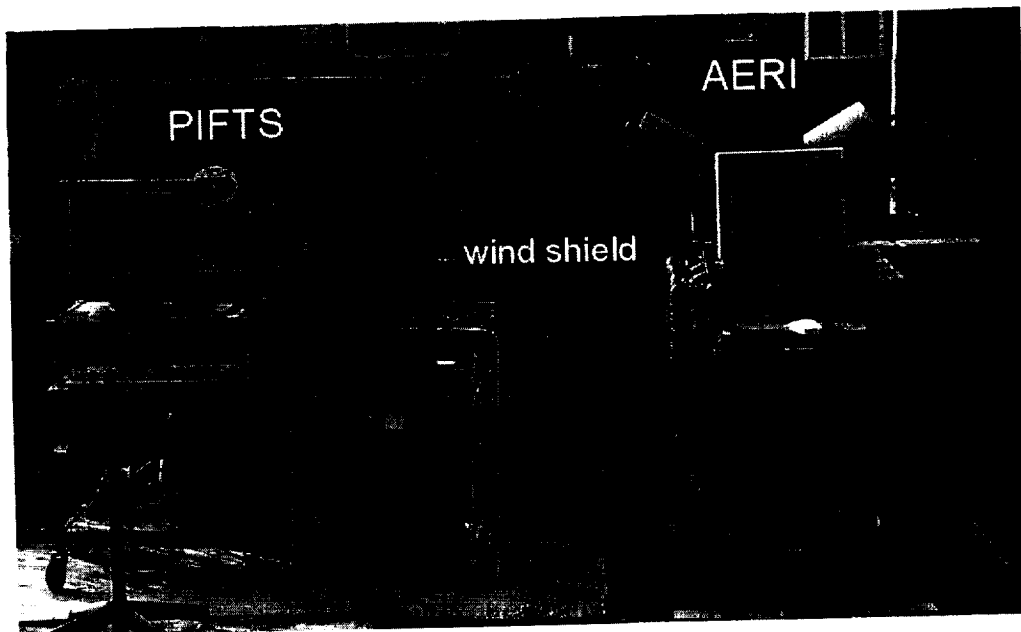
Summary of Research (Final Report) on NASA Grant NAG5-10729

Performance Period: 15 April 2001 - 14 April 2002

Principal Investigator: L.A. Sromovsky

University of Wisconsin - Madison  
Space Science and Engineering Center  
1225 West Dayton Street  
Madison, WI 53706

8 July 2002



# Contents

<b>1</b>	<b>Introduction</b>	<b>3</b>
<b>2</b>	<b>Description of the PIFTS breadboard</b>	<b>3</b>
2.1	Overview. . . . .	4
2.2	Interferometer design. . . . .	6
2.3	Imaging detector array. . . . .	6
2.4	Imaging optics. . . . .	6
<b>3</b>	<b>New Characterization Results</b>	<b>6</b>
3.1	Delay Scan Servo System Characterization and Analysis . . . . .	9
3.2	Delay scale calibration for each image pixel. . . . .	11
3.3	Interpolation to a fixed wavenumber scale. . . . .	12
3.4	Characterization of Background Interferograms. . . . .	14
3.5	Defining data processing flow for producing calibrated spectral cubes. . . . .	15
3.6	Noise in Raw and Calibrated Complex Spectra. . . . .	15
3.7	Intercomparison with AERI observations. . . . .	18
3.8	Noise Measurements and Models. . . . .	20
3.9	Publications. . . . .	20
<b>4</b>	<b>References</b>	<b>20</b>

# 1 Introduction

This report describes continued efforts to evaluate a breadboard of a Planetary Imaging Fourier Transform Spectrometer (PIFTS). The PIFTS breadboard was developed under prior PIDDP funding. That effort is described in the final report for NASA Grant NAG5-6248 and in two conference papers (Sromovsky *et al.* 2000; Revercomb *et al.* 2000). The PIFTS breadboard was designed for near-IR (1-5.2  $\mu\text{m}$ ) imaging of planetary targets with spectral resolving powers of several hundred to several thousand, using an InSb detector array providing at least  $64 \times 64$  pixels imaging detail. The major focus of the development effort was to combine existing technologies to produce a small and low power design compatible with a very low mass flyable instrument. The objective of this grant (NAG5-10729) was further characterization of the breadboard performance, including intercomparisons with the highly accurate non-imaging Advanced Emitted Radiance Interferometer (AERI) (Revercomb *et al.* 1994; Best *et al.* 1997). Before describing new characterization results, we first provide needed background information describing the PIFTS breadboard.

## 2 Description of the PIFTS breadboard

### 2.1 Overview.

The PIFTS breadboard instrument consists of (1) a miniature interferometer subsystem, (2) a dewar-mounted InSb detector array with readout electronics and a camera control computer, (3) a standard IR imaging lens, (4) an optical bench that holds the subsystems in alignment, (5) timing and triggering electronics, and (6) external sources for testing system performance. The functional relationships of these components are illustrated in Fig. 1. Shaded blocks indicate components procured from commercial vendors. The lightest shading indicates the camera system, with darker shades marking the Bomem interferometer and the camera lens. The remaining elements were either borrowed or designed and fabricated at SSEC. The scene mirror, blackbody sources, standard lamps, and controllers are elements that we borrowed from other SSEC projects.

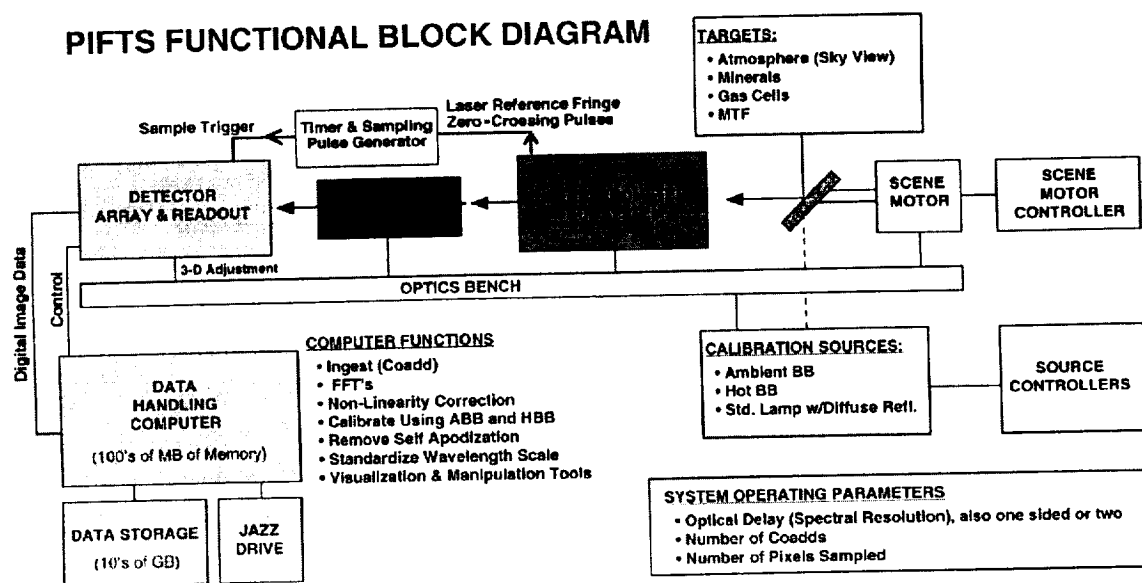


Figure 1: PIFTS breadboard functional block diagram

The interferometer package and the camera system are illustrated in Fig. 2. The small box on the left is the Bomem interferometer package, which is 5 in  $\times$  5 in  $\times$  3.5 in. The dewar on the right contains an InSb detector array, and has a commercial IR camera lens (black housing) attached on the interferometer side, and a readout electronics package attached on the right. Other support electronics and calibration hardware are illustrated in Fig. 3. The blackbody calibration sources (A and B in the figure) are of the same type as used in the AERI calibration system (Best *et al.* 1997).

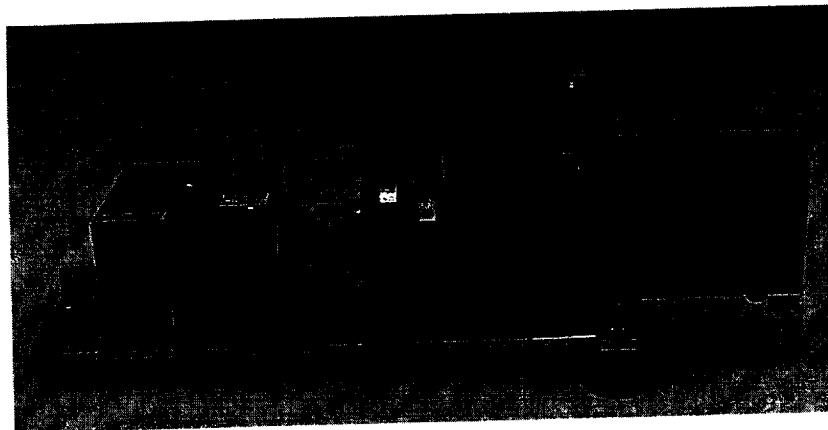


Figure 2: PIFTS modules from left to right: interferometer assembly (box), lens, detector dewar, and readout electronics, mounted on aluminum plate.

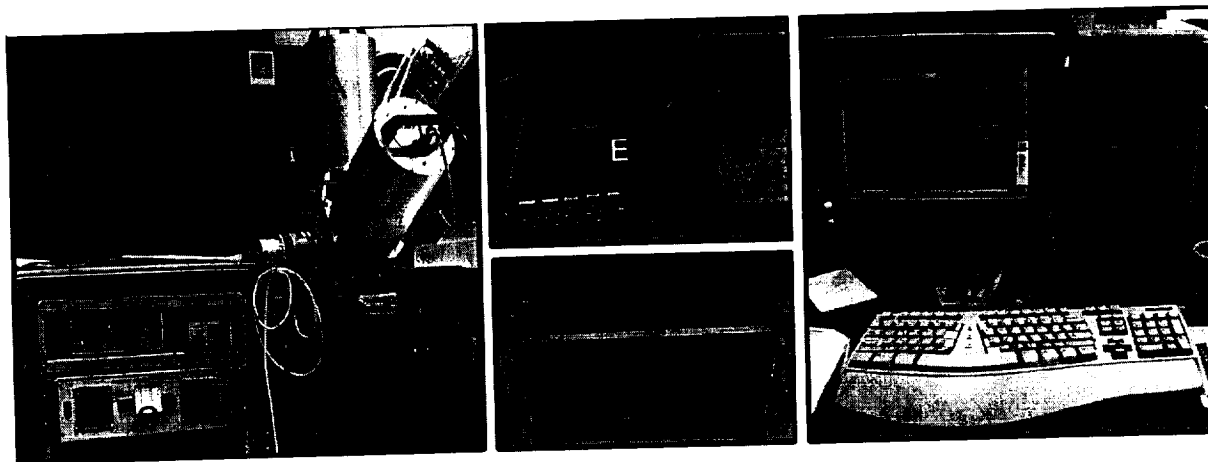


Figure 3: PIFTS support electronics: Heated (A) and ambient (B) blackbody cavities, blackbody controller (C), interferometer scan drive and metrology electronics (D), timer/controller board (E), and camera control computer/data system (F).

## 2.2 Interferometer design.

The details of the interferometer design are illustrated in the photo and drawing in Fig. 4. The input beam enters through an aperture on the left face, is divided into two beams by a  $\text{CaF}_2$  beamsplitter (mounted at  $45^\circ$  to the input axis), which are recombined after reflection from the two corner cubes, and exits near the bottom left (at  $90^\circ$  to the input). The shaded wishbone supports the two corner cube reflectors that provide differential delay scan when the wishbone pivots under control of the

### PIFTS INTERFEROMETER MECHANISM

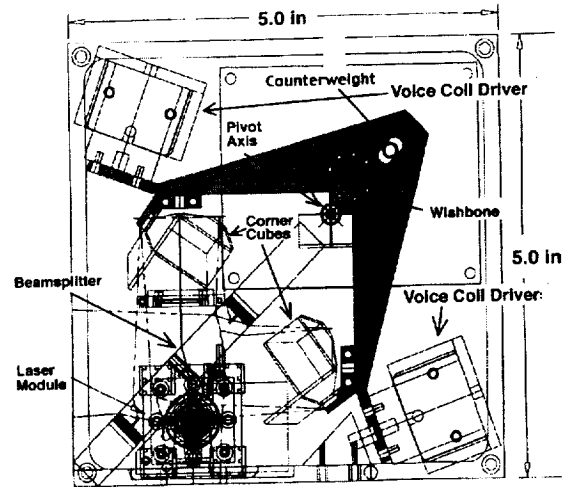
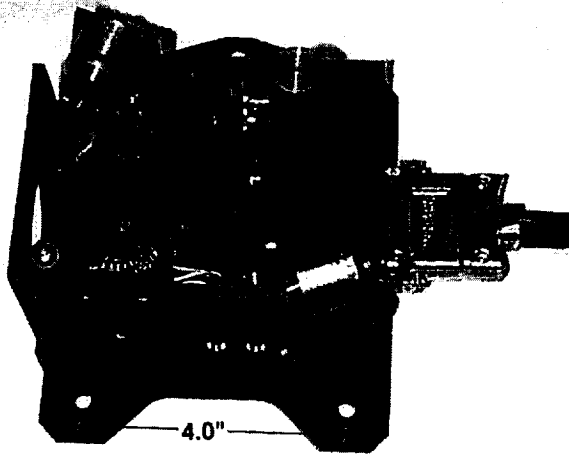


Figure 4: PIFTS interferometer assembly interior mechanism photograph (left) and mechanical drawing top view (right), for which the input from the scene is at the left and the output to the lens is at the bottom.

two voice-coil drivers. In a standard Michelson configuration, there is one fixed mirror and a second movable mirror to produce an optical path difference between the two beams. Our use of corner cubes removes the need for precise alignment of the mirrors. The optical delay is measured by monitoring the fringe intensity of a diode laser, using a retarder plate on one path so that detectors with polarizers can keep track of absolute fringe counts in either scan direction. The scan drive system uses the detected laser fringe signal as feedback to maintain a constant delay scan and to provide zero crossing pulses that are used to control the camera integration timing.

At its highest resolution, the data volume produced by PIFTS is substantial. For our laser wavelength of 852 nm ( $11,737 \text{ cm}^{-1}$ ) and two samples per fringe (one at upward zero crossing and one at each downward crossing), the max optical delay scan from  $-0.4 \text{ cm}$  to  $+0.4 \text{ cm}$  generates 18,779 frame synchronizing pulses per double-sided interferogram. For  $64 \times 64$  pixels and two signal bytes per pixel, we obtain 153.8 MB of image data per scan. At a scan rate of 500 laser fringes/sec (1000 image frames/sec), the 0.8-cm scan takes 18.79 seconds and provides a maximum unapodized spectral resolution of  $1/(2 \times 0.4 \text{ cm}) = 1.25 \text{ cm}^{-1}$ , corresponding to very respectable resolving powers of 1600 at  $5 \mu\text{m}$ , and 8,000 at  $1 \mu\text{m}$ . For applications requiring resolving powers of a few hundred (mineral or frost identification for example) delay scans can be shortened dramatically.

A relatively large beam-splitter is used to accommodate the expanding FOV of the imaging lens. Even so, this design has 1/4 the volume of the commercial instrument. There is only a small amount of vignetting within the  $64 \times 64$  detector region for the primary input beam. However, there is significant vignetting of the second interferogram that is created by radiation entering from the direction opposite to that of the scene radiation. If the optical system had expanded in both directions from the beam splitter, and the aperture of the lens were sufficient to admit that large a beam, then the second interferogram would be formed mainly from the cold finger on which the detector is mounted. But in our configuration there is only a small region in which the backward interferogram actually is formed from the cold finger radiation (plus whatever reflects off the optical elements). The outer part of the field of view actually sees background radiation emitted from the lens mount and the interferometer case (more information on this topic is provided in Section 3.4).

### 2.3 Imaging detector array.

The detector array and readout electronics were purchased as an integrated IR camera system from Santa Barbara Focalplane. The camera uses an InSb array of  $320 \times 256$  pixels, providing a  $128 \times 128$  subarray of 99.5% operable pixels, snapshot readout at 60-Hz frame rates, adjustable windowing to  $128 \times 64$  and smaller subarrays that can be read at  $> 1$  kHz frame rates, a user replaceable cold filter, detector response from  $1-5 \mu\text{m}$  (currently limited to  $3-5 \mu\text{m}$  by the cold filter and imaging lens), externally triggerable sampling, and 2-channel readout electronics with 14-Bit A/D Converters. A read noise of 400 electrons is claimed to be possible, but with the multiplexer included with our detector, and at the high read rates we needed for interferometer compatibility, we obtained a read noise of  $\sim 2400$  electrons. Detector elements are positioned on a  $30\text{-}\mu\text{m}$  square grid, with each element isolated by  $3\text{-}\mu\text{m}$  channels, yielding an effective area of  $26 \mu\text{m} \times 26 \mu\text{m}$ . This reduces the active-area quantum efficiency of  $\sim 89\%$  to an effective value of  $\sim 57\%$ . The positive benefit of the isolation channels is relatively low crosstalk.

### 2.4 Imaging optics.

We selected a relatively inexpensive standard commercial lens sold by Diversified Optics: a 25-mm focal length  $f/2.3$  4-element Si-Ge lens limited to operation in the  $2-5 \mu\text{m}$  range by the lens design and materials. Among standard IR camera lenses this lens also provides the maximum angular FOV and array coverage (longer focal length lenses have too large an entrance pupil). The exit pupil of this lens is located within the dewar, and serves as the cold aperture stop of the system. While this provides a distinct noise advantage, and allows for use of interchangeable lenses, it results in a larger lens configuration than would be preferred for a flight configuration. The detector dewar was delivered with a cold stop diameter of 0.525 inches, placed at a distance of 1.03 inches from the FPA, resulting in a slightly larger effective  $f/\#$  than the lens was designed for ( $f/2$  rather than  $f/2.3$ ). The selected lens provided a total diagonal field of view of  $6.22^\circ$  on the  $64\text{-pixel} \times 64\text{-pixel}$  subarray.

## 3 New Characterization Results

### 3.1 Delay Scan Servo System Characterization and Analysis

Extreme sensitivity of the PIFTS delay scan servo to external vibrations motivated us to better understand the servo system with the aim of improving its performance in field operations. We also wanted to investigate ways to reduce power consumption, something that would be important for a version of the instrument to be used on a space mission.

The PIFTS metrology system provides  $x$  and  $y$  outputs from the laser fringe detectors. A linearly polarized laser beam is injected into the interferometer, one arm of which introduces a  $1/4$  wave delay that converts the beam in that leg to one of circular polarization. The output detectors view orthogonal ( $x$  and  $y$ ) polarizations of the interference of the linear-polarization beam from one arm with the circular-polarization beam from the other arm. This results in the  $(x, y)$  vector tracing out an approximately circular Lissajous pattern with the angle of rotation being proportional to absolute delay. These signals are processed by a Digital Signal Processor (DSP) to compute an error signal which is subsequently fed to a compensator circuit that generates drive voltages to the voice coil drivers. The drive voltage is determined by an analog circuit that includes terms related to the position difference (between desired and measured delays), the rate of change of the difference, and the integrated difference. Thus we modeled the servo system as a forced harmonic

oscillator with the following equation of motion:

$$(J + D^2 + CD + K_m)\theta_o(t) = (K + KC_2D + KK_1D^{-1})[\theta_i(t - t_d) - \theta_o(t - t_d)], \quad (1)$$

where  $D = d/dt$ ,  $D^2 = d^2/dt^2$ ,  $D^{-1} = \int dt$ ,  $J$  is the moment of inertia of the wishbone,  $C$  is the natural damping time (with the servo turned off),  $K_m$  is the mechanical spring constant,  $K$  is the overall servo gain (torque/unit position error),  $KC_2$  is the servo gain constant for speed errors,  $KK_1$  is the servo gain for integrated position error,  $\theta_i$  is the input (desired) angular position,  $\theta_o$  is the output (actual) angular position, and  $t_d$  is the time delay between the applied torque (the RH side of the equation) and the error used to compute the applied torque ( $\theta_i - \theta_o$ ). The Laplace transform of this equation, ignoring boundary conditions, is given by

$$(Js^2 + Cs + Km)\theta_o(t) = (K + KC_2s + KK_1/s) \exp(-t_d s) [\theta_i(t) - \theta_o(t)] \quad (2)$$

where  $s$  is the complex angular frequency. From this we obtain the open and closed loop transfer functions

$$\Phi_O = \frac{(K + KC_2s + KK_1/s) \exp(-t_d s)}{Js^2 + Cs + Km} \quad (3)$$

$$\Phi_C = \frac{\Phi_O}{1 + \Phi_O} = \frac{(Ks + KC_2s^2 + KK_1) \exp(-t_d s)}{Js^3 + (C + KC_2 \exp(-t_d s))s^2 + (K_m + K \exp(-t_d s))s + KK_1 \exp(-t_d s)}. \quad (4)$$

There are three poles of the closed loop transfer function. The two off axis poles in the complex  $s$ -plane correspond to resonant frequencies, with frequency proportional to the imaginary ( $y$ ) coordinate and damping time inversely proportional to the negative real ( $x$ ) coordinate. The poles must be in the negative half complex plane of  $s$  for the control system to be stable. A positive real coordinate implies exponential growth instead of damping. Increasing gain ( $K$ ) or the time delay ( $t_d$ ) moves the poles towards instability.

We carried out a number of tests to establish mechanical properties of the drive mechanism, including natural spring constant, and natural resonant frequencies. We also measured parameters of the servo control system, including control constants for position, derivative, and integral feedback terms. We found that the most important parameter limiting servo gain was the time delay between a servo error and the application of a correction signal. About 1 ms of delay occurred in the DSP used to compute the error signal, and about 0.25 ms resulted from the inductance of the drive coils. The servo model that roughly agrees with the PIFTS characteristics is shown in the left panel of Fig. 5. The measured fractional control error is an approximation based on measuring the maximum amplitudes of perturbations that did not result in loss of servo control. For these measurements the interferometer assembly was placed on a foam pad and excited at a succession of fixed frequencies by using a solenoid to push on a corner of the housing, resulting in a combination of twisting and lateral acceleration perturbations, which were measured by a linear accelerometer. The accelerations were converted to displacement amplitudes by dividing by  $(2\pi f)^2$ . We then normalized by the displacement at middle frequencies beyond the range of servo control. The disagreement in the location of the resonant dips of the model and the measurements is probably due to the fact that the foam pad also has a resonance. The discrepancy at very low frequencies might also be due to a change in the fraction of the perturbation that results in a rotational displacement.

A model with a weaker spring and shorter delay time is shown in the right panel of that Fig. 5. We found that the servo gain could not be increased beyond the value chosen by BOMEM without making the servo extremely unstable, and we in fact decided to reduce the gain somewhat to make it more stable. We found that servo control was limited to frequencies below about 100 Hz, and that the best solution to improving field performance was to limit high frequency inputs with compliant shock mounts and wind shielding.

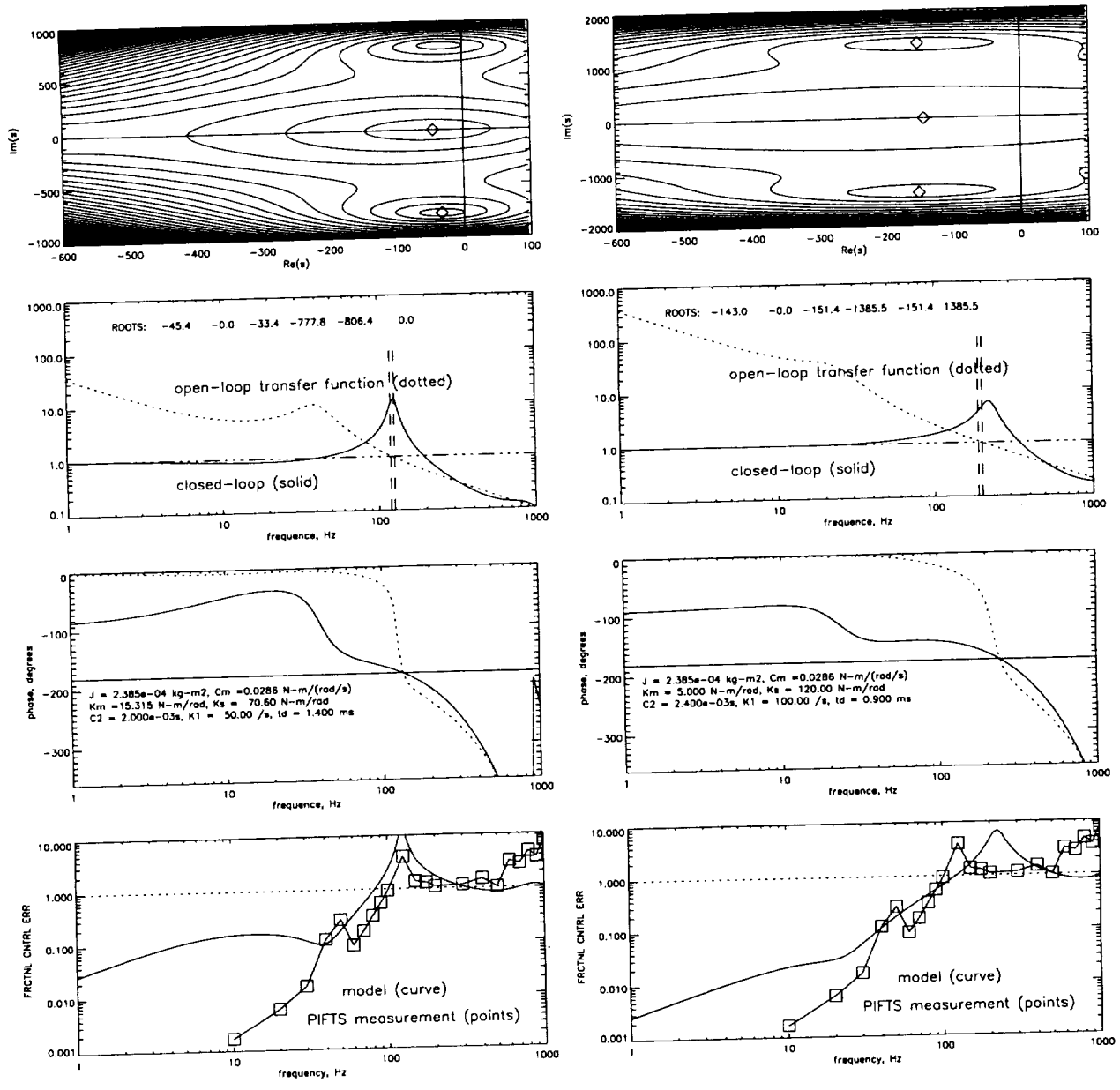


Figure 5: Servo model characteristics approximating nominal PIFTS configuration (left) and improvements possible with reduced delay time, reduced mechanical spring constant, and increased servo gain. The top plot displays the three poles in the closed loop transfer functions, the second provides open and closed loop transfer functions, the third provides the corresponding phases, and the bottom curve provides the control error. Approximate measured control errors for the nominal PIFTS configuration are shown as plotted points.

The main reason for the high power consumption of the servo was the use of very stiff return springs on the wishbone assembly. The position term of the servo also acts like a mechanical spring, except that the mechanical spring has no time delay. Thus, if we eliminate or greatly reduce the mechanical spring constant, we may not be able to compensate for it by increasing the

servo gain, unless we can also reduce the time delay in generating a correction signal. Fortunately, the mechanical spring is actually much less stiff than the servo itself, so there is potential to reduce power consumption, without greatly changing drive system performance. However, greatly reducing spring stiffness would require modification of the initialization sequence used to establish servo lock at instrument startup.

We also found resonances in the wishbone structure, although at relatively high frequencies that would not be excited much with proper shock mounting and shielding. The wishbone tuning fork vibration mode had a resonant frequency of about 621 Hz, while a second resonance near 856 Hz seems to be associated with a flexing of the corner cube mount.

### 3.2 Delay scale calibration for each image pixel.

Every pixel in the PIFTS interferogram data cube has a slightly different delay scale associated with its corresponding interferogram. The delay scale is a function of the angle the pixel makes with respect to the optic axis. If we knew the laser wavenumber precisely, this would be reduced to a problem of finding the pixel coordinates of the optic axis and the off axis angle of each pixel. We can't assume that the off axis angle can be computed from the focal plane geometry and the focal length of the imaging system, because the focal length of the lens is not known that well.

We first determined  $\lambda_{\text{eff}}$  at each of 25 locations on the focal plane array. For each location, we varied  $\lambda_{\text{eff}}$  from 0.998 to 1.002 times the nominal value of 852 nm, and computed  $\chi^2$  as a function of  $\lambda_{\text{max}}$ . We computed  $\chi^2$  over the wavenumber range 2050  $\text{cm}^{-1}$  to 2150  $\text{cm}^{-1}$  by evaluating the sum

$$\chi^2 = \Sigma(L(\nu)_{\text{AERI}} - L(\nu)_{\text{PIFTS}})^2 / \sigma(\nu)^2, \quad (5)$$

where  $L$  denotes radiance spectrum, and  $\sigma^2$  is the expected variance in the radiance difference. We expect the radiance difference to be dominated by noise in the PIFTS radiances, which was measured to be about 0.075-0.08 radiance units ( $ru = \text{mW}/(\text{m}^2\text{-sr}\text{-cm}^{-1})$ ) for individual samples. For the averages of 79 samples that we used, we would have expected PIFTS radiance errors to be less than 0.01  $ru$ . The AERI noise contribution is only about 0.005  $ru$ , suggesting that the combined variance should be no more than  $(0.011 \text{ } ru)^2$ . However, to make the  $\chi^2$  minimum equal to the number of samples less the number of fitted parameters, we would need a  $\sigma$  of about 0.04  $ru$ . The best we were able to obtain from comparing PIFTS and AERI spectra was an RMS difference of about 0.02 radiance units, and in the 2050 - 2150 wavenumber region we observed some systematic differences between the two instruments, that may have limited the noise reduction that could be obtained by averaging. It might also be possible that averaging over a circular region about the central pixel would distort the spectrum somewhat, which would also limit the minimum value of the difference spectra. Even with the larger than expected noise in the difference spectra, we had more than enough information to constrain the parameters of our model. Plotting  $\chi^2$  as a function of  $\lambda_{\text{eff}}$ , we obtained well defined quadratic minima (Fig. 6 for example). The wavenumber difference that increased  $\chi^2$  by one unit was taken as the uncertainty in  $\lambda_{\text{eff}}$ . For each of 25 locations on the focal plane array the fractional uncertainty in  $\lambda_{\text{max}}$  was within the range of 6-6.5E-6, or 0.0051-0.0055 wavenumbers.

After determining the 25 best-fit values of  $\lambda_{\text{eff}}$ , we then used non-linear regression to constrain the values of our model of  $\lambda_{\text{eff}}$ . We can express  $\lambda_{\text{eff}}$  as a function of pixel position  $(x, y)$  in terms of four adjustable parameters:

$$\lambda_{\text{eff}}(x, y) = \lambda_{\text{max}} \cos(\arctan([(x - x_o)^2 + (y - y_o)^2]^{1/2} / f_p)), \quad (6)$$

where  $(x_o, y_o)$  are the optic axis coordinates in pixels,  $\lambda_{\text{max}}$  is the laser wavelength at the optic axis, and  $f_p$  is the focal length in pixel units. The parameters of the model were individually varied

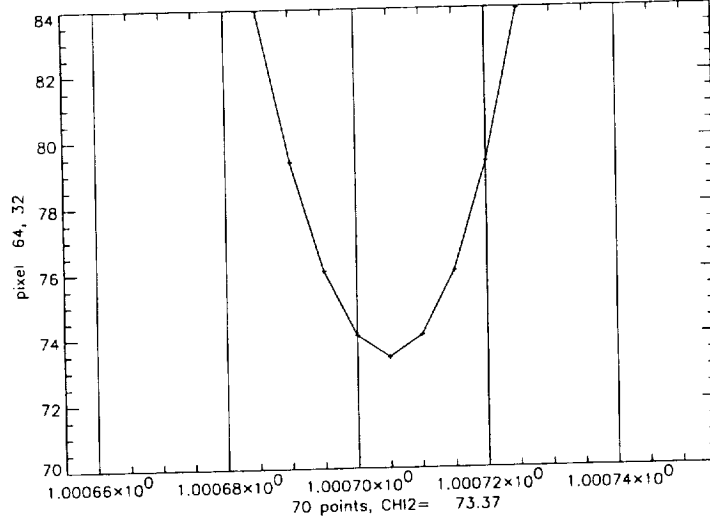


Figure 6:  $\chi^2$  as a function of a scale factor that is the ratio of trial laser wavelength to the nominal laser wavelength of 852 nm, shown for average centered at image coordinates (64, 32).

step by step over a range of values. At each value, the other parameters were adjusted to obtain the smallest value of  $\chi^2$  at that value of the parameter of interest. The resulting plots of  $\chi^2$  were rescaled so that the minima were equal to the number of degrees of freedom (21 in this case) and the value change producing a  $\chi^2$  increase of 1 defined the uncertainty for that parameter. The results were as follows:

$$\begin{aligned}
 x_o &= 67.084 \pm 0.029 \text{ pixels} \\
 y_o &= 42.264 \pm 0.045 \text{ pixels} \\
 \lambda_{max} / 852 \text{ nm} &= 1.0007797 \pm 1.6\text{E-}6 \\
 (\lambda_{max} &= 852.6643 \text{ nm} \pm 0.0014 \text{ nm}) \\
 (1/\lambda_{max} &= 11,727.945 \text{ cm}^{-1} \pm 0.019 \text{ cm}^{-1}) \\
 f_p &= 1/(0.00120088 \pm 1.53\text{e-}6) = 832.72267 \pm 1.06 \text{ pixels}
 \end{aligned}$$

For a pixel pitch of 30  $\mu\text{m}$ , this implies a focal length of 24.98 mm  $\pm$  0.03 mm, compared to the nominal value of 25 mm  $\pm$  1.25 mm.

Thus we are able to find the optic axis within 0.03-0.05 pixels, the on-axis wavenumber scale to within 0.0014 nm (1.6 parts per million), and the imaging focal length to within 1.2 parts per thousand (which defines the angular scale of the image to the same precision). Slightly worse performance is expected from comparisons between PIFTS and calculated radiances.

With fits to more points on the focal plane it should be possible to define any important image distortions that may be present as well. (Most optical systems have some degree of distortion. Examples include the WFPC2 camera system on the Hubble Space Telescope and the NSFCAM imager on the NASA Infrared Telescope on Mauna Kea, which both need some correction for distortion.) Distortion corrections may be important in mosaicing of images taken at different view angles.

### 3.3 Interpolation to a fixed wavenumber scale.

It is not sufficient to establish the correct wavenumber scale for each image pixel. To facilitate data analysis algorithms that combine spectra from different pixels, it is best to put all spectra on the same wavenumber scale at the outset. Interpolation is needed, either in the spectral domain or in the delay domain. Resampling in the spectral domain can be done by first zero-filling the interferograms to several times their original length (with the optimum factor depending on the degree of oversampling in the original interferogram), then transforming to the spectral domain, which produces a highly oversampled spectrum that can be easily interpolated at the desired spectral sampling. To facilitate analyses of data from different cubes, or different days, for which the reference laser wavelength might be slightly different, it is best to put all observations on a standard wavelength scale. The interpolation quality improves with the length of the zero fill, but the time to do the FFT increases as  $N \log(N)$ .

Current PIFTS interferograms are significantly oversampled relative to the Nyquist criterion: with 23,473 samples/cm, we obtain 11.7 samples per signal fringe at  $5 \mu\text{m}$  and 7 samples per fringe at  $3 \mu\text{m}$ . Thus, it is possible to do a reasonably accurate interpolation in the delay domain. We compared transforms of linear and cubic spline interpolations with the transform of a factor-of-8 zero-fill interferogram, which we use as a standard. The errors of a cubic spline interpolation (Fig. 7) are less than 0.1% from  $1980 \text{ cm}^{-1}$  to  $3100 \text{ cm}^{-1}$ , and 0.02% or less in the lower noise regions of the spectrum from  $2000 \text{ cm}^{-1}$  to  $2900 \text{ cm}^{-1}$ . Linear interpolation errors are typically a factor of 100 worse than this. The cubic spline errors may be even smaller than our analysis has so far indicated. In high-noise regions, the inherent smoothness of the spectrally band-limited signal is contaminated by random noise variations that are only band-limited by the digital averaging window, which is harder to reproduce with the same percentage accuracy. The overall performance of the cubic spline interpolation is more than adequate.

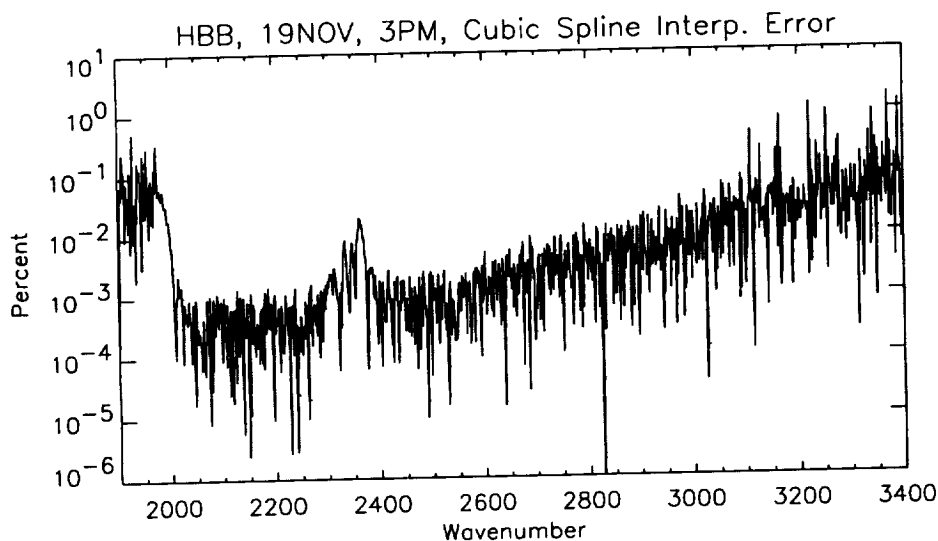


Figure 7: Cubic spline interpolation errors, using a noisy PIFTS spectrum with the transform of an  $8 \times$  zero-fill padded interferogram as the spectral reference.

### 3.4 Characterization of Background Interferograms.

Half of the radiation entering the input aperture of the interferometer is reflected back toward the source. It is also true that half of the radiation entering from the exit aperture (and surroundings) is reflected back towards the detector. This background interferogram has been modeled and demonstrated to have a modulation that is inverted relative to the modulation of the interferogram generated by the incoming beam. A comparison of beam combinations leading to the normal scene view interferogram and the background interferogram is shown in Fig. 8. Actually, for the PIFTS and AERI instruments the interferogram modulation produced by the incoming beam is negative while the modulation of the background interferogram is positive. This can be inferred from the analysis on pages 4 and 5 of Brault (1985), with one modification. For one of our recombined beams, the beam-splitter reflection is internal, while for the other it is external, resulting in a relative  $180^\circ$  phase shift between them that produces a negative modulation. In Brault's analysis the recombined beams each have one external reflection, leading to positive modulation. Besides the different sign of modulation of the interfering beams entering from the rear, the background amplitude also has a different value, although not significantly different. Assuming that the beam-splitter reflectivity  $R_B$  and transmission  $T_B$  satisfy  $R_B = 1 - T_B$ , we can write the relative interferogram amplitudes of these two sources as,

$$I_1(x) = KR_m R_B T_B [1 - \cos(2\pi x\nu + \phi_1)] L_1(\nu) \quad (7)$$

$$I_2(x) = KR_m R_B T_B \left[ \frac{R_B^2 + T_B^2}{2R_B T_B} + \cos(2\pi x\nu + \phi_2) \right] L_2(\nu) \quad (8)$$

where  $R_M$  is the reflectivity of either beam-return mirror and  $K$  is a common proportionality constant. It can also be shown that they have the same compensation, so that they should have the same uncompensated phase errors, although the equation is written to include the possibility of some other anomalous phase.

The net signal seen by the detector is the sum of the two interferograms. The observed modulated interferogram is thus the sum of two components and the transform of the interferogram becomes

$$\int_{-\infty}^{\infty} I(x) \exp(2\pi i\nu x) dx = G_1(\nu) - G_2(\nu) \quad (9)$$

where we use  $G_1$  to denote the signal spectrum of the target, while  $G_2$  denotes the spectrum of the instrument. If one attempts to determine a spectrum  $G(\nu) = |G(\nu)| \exp(i\phi) = G_1(\nu) - G_2(\nu)$ , the resulting phase can be wildly variable at wavenumbers for which the two component spectra have similar values, and thus lead to sign flips. At the center of the instrument FOV, the background arises mainly from the cold regions inside the dewar, and is relatively low. But off axis pixels see larger and larger background contributions, which can even exceed the amplitude of the primary interferogram. The interference of these two interferograms leads to large phase variations across the instrument field of view. Complex calibration equations (Revercomb *et al.* 1988; Sromovsky 2002) are successful at removing the background contributions, and allow us to define the characteristics of the background as well as the responsivity of the system. The background radiance image can be expressed as

$$L_2 = \frac{G_c L_h - L_c G_h}{G_h - G_c} e^{i(\phi_1 - \phi_2)} \quad (10)$$

where  $\phi_1$  is the phase of "normal" spectrum and  $\phi_2$  is the phase of the background spectrum, and subscripts  $c$  and  $h$  refer to cold and hot reference observations. The real portion of the background radiance spectrum, converted to brightness temperature, is shown in Figure 9. The image is an average over the  $2100\text{-}2200 \text{ cm}^{-1}$  spectral range.

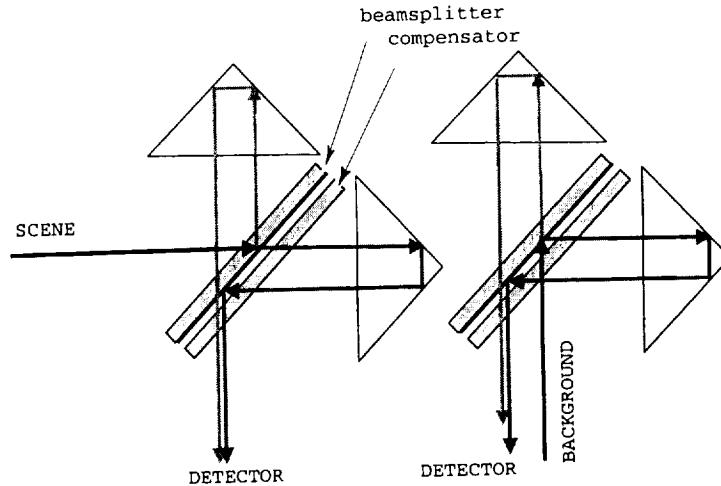


Figure 8: Beam combinations leading to interferograms of the scene (left) and the background (right). Note that one of the background beams is externally reflected by the beam-splitter multilayer reflective coating (dark line facing the air gap), while for the primary interferogram, one beam has an internal and one an external reflection from that coating. This is the source of the relative phase change between the two modulations.

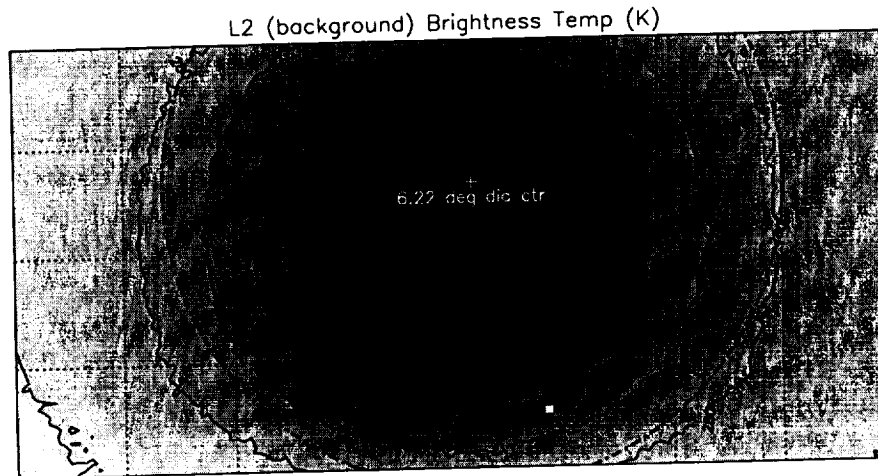


Figure 9: Background radiance field (real part), shown as brightness temperature averaged over  $2100\text{-}2200\text{ cm}^{-1}$ . The dot-dash circle indicates the  $6.22^\circ$  unvignetted PIFTS FOV through the entrance aperture. The reflected view through the exit aperture is vignetted by the background structure at angles determined mainly by the relatively small exit aperture.

If there were no vignetting, and no reflection from optical elements between the interferometer and focal plane array, we would expect a relatively uniform brightness temperature around  $77\text{ K}$ , the temperature of the  $\text{LN}_2$ -cooled array. Instead we see a retrieved brightness temperature of  $250\text{ K}$  at the center of the image, which can be obtained by a linear combination of  $70\%$  emission at  $77$

K and 30% emission at the ambient temperature of 283 K.

### 3.5 Defining data processing flow for producing calibrated spectral cubes.

This summarizes the flow of information in our processing of PIFTS dat from raw data acquisition through creation of calibrated scene spectra.

1. Measure a set of detector signals at delay steps  $\Delta x$ , as the interferometer is scanned from nominal delay  $-X_1$  to  $+X_1$ , in which delay is measured relative to a reference laser that may be sampling an angular position different from that sampled by the scene interferogram detector. Let this set of readings be  $V_k, k = 0, N_1 - 1$  at nominal delay positions  $x_{1,k}, k = 0, N_1 - 1$ .
2. Re-scale the delay values to account for the off-axis angle of the detector relative to the laser reference, and for any other related scale changes.
3. If this is a hot blackbody measurement find the zero delay position by locating the extreme value of the interferogram (this could be taken as the extreme value, or use a fit to the extreme value and its neighbors to find an interpolated peak). If this is not a hot blackbody measurement, then use the last determination of the zero delay position (which must have been done since the interferometer last lost servo lock).
4. Interpolate all interferogram values to a standard set of delay positions so that both interferograms and spectra for different detector elements in an image can be directly compared or averaged. This will result in a new set of  $N$  interferogram values  $V(x_k)$  at delay values  $x_k, k = 0, N - 1$  from  $-L$  to  $+L$ , where  $N < N_1$  and  $L < X_1$ . Shifting and symmetrizing the delay range necessitates some loss of data.
5. Subtract the mean and linear ramp, then flip the sign to get a modulation signal that is positive at zero delay. The result will be called  $V_I(x_k)$  which is some constant  $K$  times the modulated part of the interferogram radiance (defined in Eq. 3 of Sromovsky 2002).
6. Create a re-ordered array  $V_s(x) = \begin{cases} V(x) & \text{for } x = 0, \dots, L \\ V(x - 2L) & \text{for } x = L, \dots, 2L \end{cases}$
7. Multiply by  $\frac{2L}{N}$  to get  $h_k = \frac{2L}{N}V_s(x_k), k = 0, \dots, N - 1$
8. Carry out discrete FFT to obtain  $H_n, n = 0, \dots, N - 1$

9. Reorder  $H_n$  to get  $KH(\nu_n) = \begin{cases} H_n & n = 0, \dots, N/2 - 1 \\ H_{n+N} & n = -N/2, \dots, -1 \end{cases}$ , where  $H$  is the complex spectral function obtained from the convolution

$$H(\nu) = G(\nu) * 2L\text{sinc}(2L\nu),$$

where

$$G(\nu) = \begin{cases} \frac{1}{2}B(\nu) \exp(i\phi_\nu) & \text{for } \nu > 0 \\ \frac{1}{2}B(-\nu) \exp(-i\phi_{-\nu}) & \text{for } \nu < 0 \end{cases},$$

and where  $K$  is the conversion between spectral radiance units and measured units (DN or voltage). If this is a hot or cold blackbody measurement, save this result as the complex spectrum  $KH_h$  or  $KH_c$ . Otherwise, proceed to the next step.

10. If this is a complex scene spectrum, then compute a calibrated spectrum as

$$L = L_c + \frac{KH - KH_c}{KH_h - KH_c}(L_h - L_c).$$

Set  $L$  equal to  $Re(L)$  to insure that imaginary components introduced by errors are eliminated. Note that this spectrum will be the true spectrum convolved with a sinc function, provided that both  $\phi_\nu$  and  $\eta(\nu)$  are sufficiently slowly varying that the following approximation is valid:

$$\int_{-\infty}^{\infty} \eta(\nu')L(\nu') \exp(i\phi_{\nu'}) \text{sinc}(2(\nu - \nu')L) d\nu' \approx \eta(\nu) \exp(i\phi_\nu) \int_{-\infty}^{\infty} L(\nu') \text{sinc}(2(\nu - \nu')L) d\nu'.$$

11. Compute responsivity using

$$R = \frac{|KH_h - KH_c|}{L_h - L_c}$$

An internal report (Fry 2002) illustrates these steps in great detail. Further details concerning the calibration process are discussed in a paper submitted to *Applied Optics* (Sromovsky 2002).

### 3.6 Noise in Raw and Calibrated Complex Spectra.

Complex calibration is required to properly eliminate the effects of phase errors, complex background signals, and anomalous phase errors due to beam-splitter emissions. The basis for complex calibration, and a discussion of the effects of complex calibration on noise is provided in a paper submitted to *Applied Optics* on 29 March 2002 (“Radiometric Errors in Complex Fourier Spectrometry” by L. A. Sromovsky). The error in the calibrated radiances depends on the error in the calibration measurements, the uncertainty in the source radiances, and the error in the scene radiance measurement. The relationship between these quantities is as follows:

$$\sigma_{LS}^2 = m^2 \sigma_V S^2 + [\sigma_{LC}^2 + m^2 \sigma_{VC}^2] ((L_h - L_s)/(L_h - L_c))^2 + [\sigma_{LH}^2 + m^2 \sigma_{VH}^2] ((L_s - L_c)/(L_h - L_c))^2 \quad (11)$$

where  $\sigma_{VS}$ ,  $\sigma_{VC}$ ,  $\sigma_{VH}$ , are the standard errors in measuring the detector voltage (or DN) signals in response to scene, cold blackbody, and hot blackbody references, where  $m = (L_h - L_c)/(V_h - V_c)$  is the slope of the calibration line used to convert voltage (or DN) to radiance, and where  $\sigma_{LC}$  and  $\sigma_{LH}$  are the uncertainties in the radiance values of the two reference sources. The expected noise varies with scene radiance. The minimum variance in calibrated radiances is found for scene radiances between the two reference radiances; the variance grows quadratically away from the minimum.

The importance of complex calibration is shown to be especially great when background interferogram amplitudes are comparable to primary interferogram amplitudes. Because the sign of the background modulation is opposite to that of the scene interferogram, phases can be wildly varying where net amplitudes are small due to cancellation, leading to poorly behaved magnitude spectra. Complex calibration eliminates this problem.

### 3.7 Intercomparison with AERI observations.

Preliminary comparisons were made between PIFTS and AERI observations on 19 November 2001. Both instruments were placed in close proximity outside our building (Fig. 10) and arranged to put the AERI field of view within the PIFTS field of view, as shown in Fig. 11. We also launched

a radiosonde from the top of our building to provide data needed for calculating the radiance field under observation. November 19 was a day with apparently clear and photometric skies, but generally high winds required us to use a wind shield (Fig. 10) to keep the PIFTS delay scan servo from occasionally losing lock. The high winds also resulted in rapidly increasing radiosonde range after release, and resulting loss of contact with the radiosonde at a relatively low altitude. Although this radiosonde only returned data up to 10.95 km, the radiance contributions above this level have been shown to be negligible for a clear atmosphere, thus providing sufficient atmospheric information to permit accurate line-by-line spectral radiance calculations. Prior observations on 15-16 November were less wind-perturbed, had better vertical coverage by radiosondes, but contained a small degree of cirrus cloud contamination, which might complicate comparisons with radiation transfer calculations. These observations were also noisier than those on 19 November.

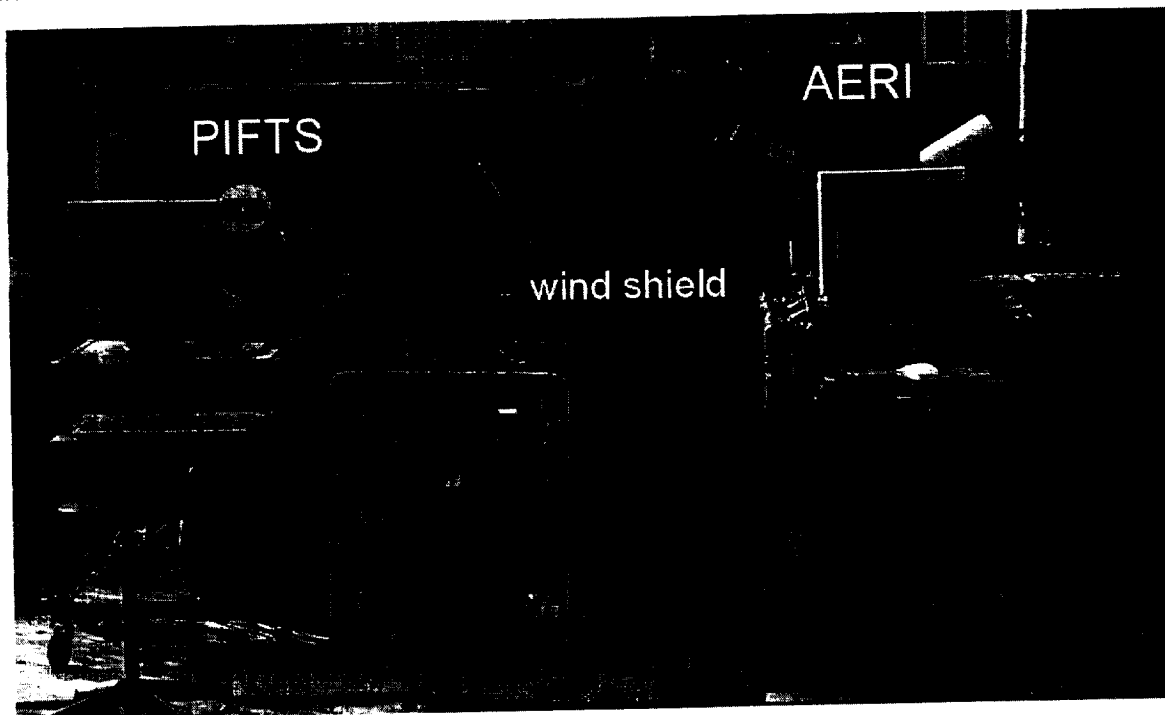


Figure 10: PIFTS and AERI configured for intercomparison test in the yard next to the Space Science and Engineering Center on the UW Madison campus.

The PIFTS spectra that were used in the initial 19 November comparison were really only in preliminary form. Interferogram slopes had not been removed prior to calculating spectra, although sample calculations indicate that the effects of the slope are probably not significant. For the preliminary analysis, the wavenumber scale was obtained from fitting PIFTS observations averaged over the central  $9 \times 9$  subimage to AERI observations. These results are shown in Fig. 12.

PIFTS and AERI spectra from 19 November 2001 agree well with each other except between  $2300$  and  $2400 \text{ cm}^{-1}$ , where AERI results have greater errors due to longer path lengths to blackbodies in this region of extreme  $\text{CO}_2$  opacity, and between  $2080$  and  $2180 \text{ cm}^{-1}$ , for which there is no obvious explanation. Below  $2100 \text{ cm}^{-1}$  both PIFTS and AERI disagree with calculations, perhaps because water amounts during PIFTS and AERI observations were different from those reported by the radiosonde.

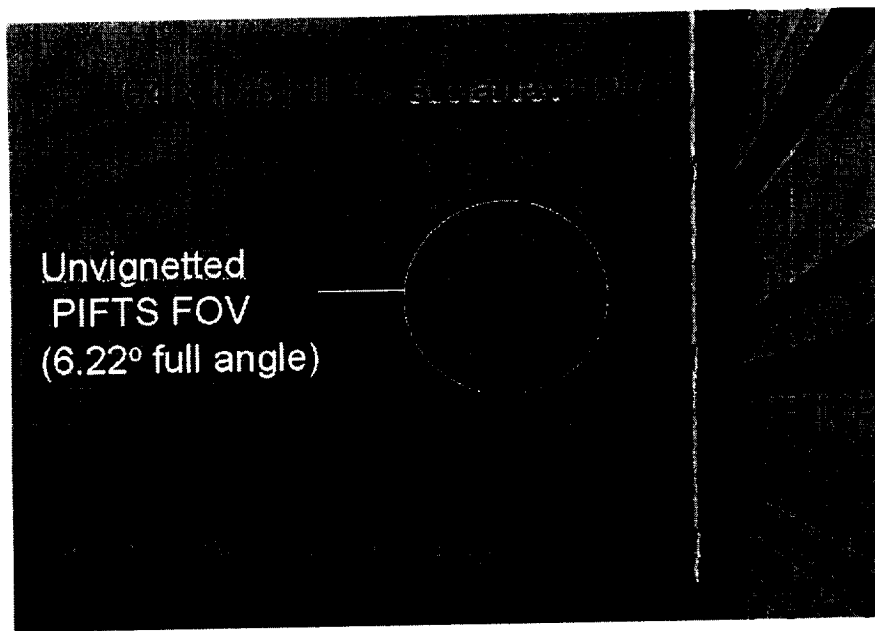


Figure 11: Comparison of PIFTS and AERI fields of view during intercomparison tests on 19 November 2001. The structure at the right is the north side of the Atmospheric, Oceanic, and Space Sciences building.

Radiance calculations made use of the LBLRTM code developed by Clough *et al.* (1991). These calculations require that radiosonde data files be sanitized to avoid negative, zero, or very small positive altitude increments that round to zero. In addition, obtaining good agreement of calculations with AERI and PIFTS measurements required adding a 1K offset to the radiosonde temperature data. Although that correction works well, there may be some other way to achieve agreement without such a large “correction” to the radiosonde data - larger than local expertise would expect. However, it is clear that just modifying the near-surface structure (i.e. below the first radiosone observation) cannot produce agreement over a broad spectral range.

After more extensive analysis, following more accurate data processing procedures for putting all observations on the same wavenumber scale (described in Section 15 and more fully in the 23 April 2002 Fry report), the above intercomparison results for 19 November 2001 remain valid. However, analysis 16 November 2001 observations revealed that the laser wavenumber had drifted 1.1 parts in  $10^4$ . With that correction we were able to obtain a PIFTS-AERI difference spectrum that had a mean value of only  $0.004 \text{ mW}/(\text{m}^2\text{-sr-cm}^{-1})$  and an RMS value of  $0.018 \text{ mW}/(\text{m}^2\text{-sr-cm}^{-1})$  over wavenumbers from  $2000 \text{ cm}^{-1}$  to  $2600 \text{ cm}^{-1}$ . The PIFTS spectrum used in this difference was an average over a 35-pixel by 35-pixel box, taken to reduce random noise contributions. The systematic errors in this difference spectrum are seen to be extremely small. The reason for the laser wavenumber change remains to be determined. The laser diode emits at a wavenumber that depends on temperature. There is a servo that maintains the laser over a narrow temperature range, although it is not clear at this point whether the servo is operating properly.

The intercomparison test was partly supported by a grant from the University of Wisconsin Graduate School.

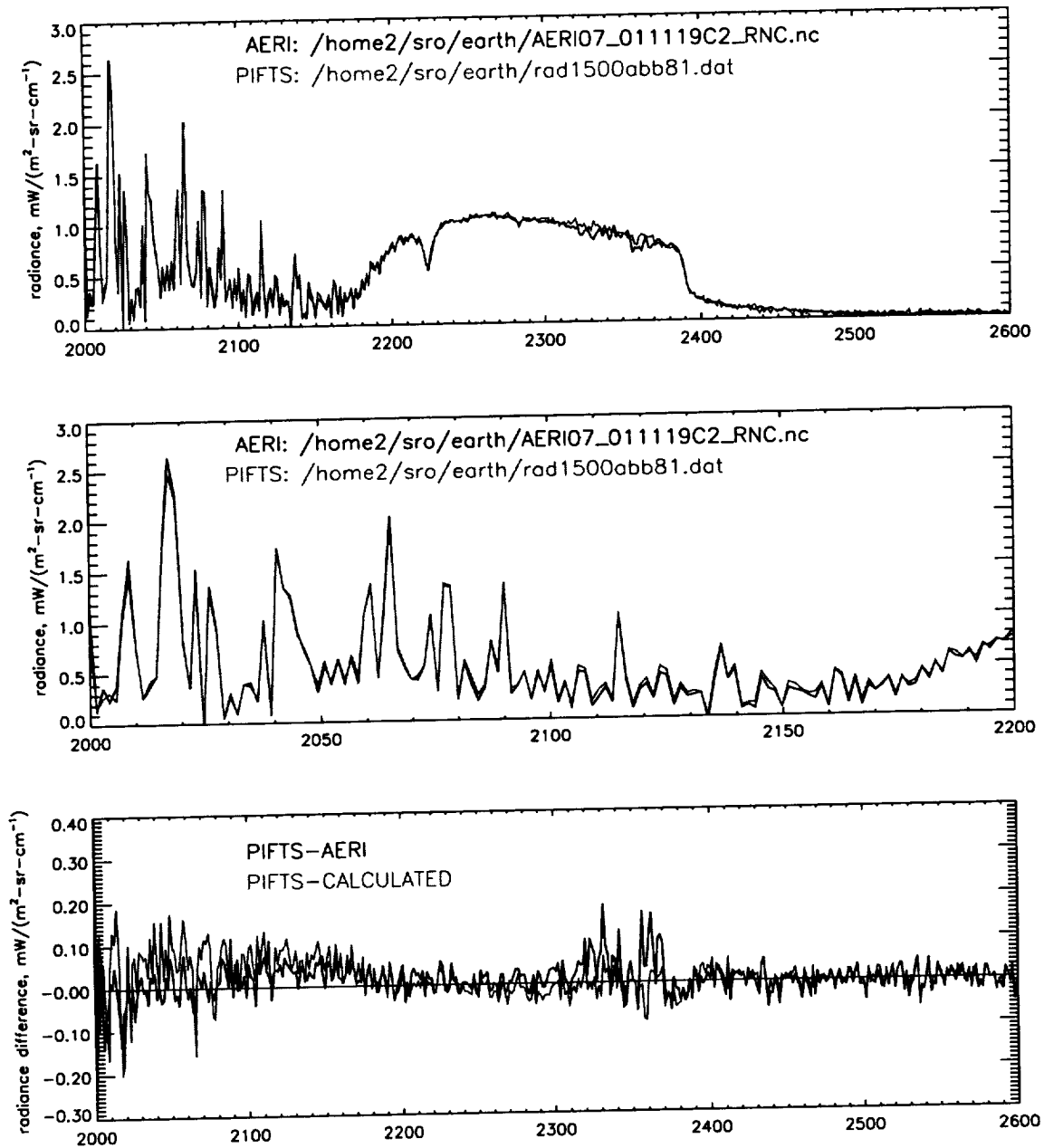


Figure 12: Comparison of PIFTS radiance from 19 November 2001 with simultaneous AERI calculations and LBLRTM calculations.

### 3.8 Noise Measurements and Models.

Random radiometric errors appear to be 0.02 to 0.04  $\text{mW}/(\text{m}^2\text{-sr-cm}^{-1})$  for PIFTS relative to calculations, and for PIFTS relative to AERI, using 9-pixel by 9-pixel averages for PIFTS. Single-pixel noise levels would be presumably 9 times larger, or 0.18 to 0.36  $\text{mW}/(\text{m}^2\text{-sr-cm}^{-1})$ , quite a large noise level in a region where typical atmospheric emitted radiance values are of the order of

1 mW/(m<sup>2</sup>-sr-cm<sup>-1</sup>) or less.

The noise levels derived for single-pixel radiances, derived from the standard deviation of individual calibrated spectra for individual pixels relative to the mean value (as described in the final report on the original PIDDP grant), are approximately 0.075-0.08 mW/m<sup>2</sup>-sr-cm<sup>-1</sup>, measured under laboratory conditions with a delay scan of  $\pm 0.174$  cm<sup>-1</sup> (unapodized resolution of 2.87 cm<sup>-1</sup>). Because NESR is proportional to  $L/\sqrt{N}$  when dwell time per sample is fixed, for a delay scan twice as long (unapodized resolution of 1.435 cm<sup>-1</sup>), the noise is increased by  $\sqrt{2}$  to 0.106-0.113 *ru*. This suggests that random detector noise contributions to a  $9 \times 9$  average should be about .012-.013 radiance units (about 1/2 to 1/3 of the PIFTS-AERI difference observed during the intercomparison on 19 November), and  $35 \times 35$  pixel averages should have negligible contributions from detector noise.

The observed rms PIFTS-AERI and PIFTS-LBLRTM differences are 0.02-0.04 radiance units, where LBLRTM are calculated radiance values using radiosonde profiles as inputs. It is hard to attribute much of this to AERI because the AERI noise level is supposed to be only 0.005 radiance units (R. Knuteson, personal communication, May 2002).

A reasonable model of rms deviations between PIFTS and AERI is as follows:

$$\sigma_{TOT}^2 = \sigma_{AERI}^2 + \sigma_{SYS}^2 + \sigma_{PIFTS}^2/N, \quad (12)$$

where  $\sigma_{AERI}$  is the rms noise in the AERI spectra,  $\sigma_{PIFTS}$  is the rms noise in the single-pixel PIFTS spectra,  $N$  is the number of pixels averaged, and  $\sigma_{SYS}$  is the systematic rms error associated with delay sampling errors, laser wavelength drifts, and other errors that affect spectra for all pixels in a given cube in the same way and are thus not reduced by averaging over many pixels.

If we estimate AERI noise from the standard deviation of 5 successive AERI spectra relative to their mean spectrum, we find a value generally closer to 0.01 radiance units, rather than the 0.005 units suggested by Knuteson. This probably includes some variability in the atmosphere as well as instrumental noise, however. If we use 0.01 units for  $\sigma_{AERI}$ , then the remaining offset variance (the value at  $N=\infty$ ) must be attributed to  $\sigma_{SYS}$ . From the 14:55 cube on 15 NOV we find good agreement with the model, using  $\sigma_{SYS} = 0.026$  *ru*, and  $\sigma_{PIFTS} = 0.243$  *ru*, the latter being established by the variation of  $\sigma_{TOT}^2$  with  $N$ . We varied  $N$  by varying the size of the PIFTS subarray that is averaged. For this cube there was a clear linear dependence of total variance on  $1/N$ . For the 13:15 cube on 19 November, which has much less noise, the dependence of  $\sigma_{TOT}^2$  on  $1/N$  does not closely follow the linear model. Rough agreement is obtained with  $\sigma_{SYS} = 0.023$  *ru*,  $\sigma_{AERI} = 0.01$  *ru*, and  $\sigma_{PIFTS} = 0.16$  *ru*. Even this lower noise level is much larger than expected. It also seems to be larger than estimated by other means.

If we average all PIFTS spectra in a subarray and compute the standard deviation of individual pixel spectra from that mean, we find larger values for intercomparison tests than expected from laboratory noise measurements when adjusted for resolution differences. The closest agreement is for the 19 Nov 02 13:15 cube, from which we obtain a minimum noise of about 0.13 *ru*, compared to the value of 0.11 *ru* inferred from laboratory results discussed previously. One of the worst disagreements is for the 16 November 15:45 cube, from which we obtain a minimum noise of 0.16 *ru*. The variation is even larger outside the 2200-2300 cm<sup>-1</sup> region of the minima. For example, at 2450 cm<sup>-1</sup>, which we expect to be close to 0.11 *ru* from lab results, ranges from 0.145 *ru* (19 Nov 13:15) to 0.18 *ru* (16 Nov 15:45). These standard deviations were computed for square subarrays, generally 35 pixels on a side.

Even more troubling is the presence of asymmetries in variability between row and column directions (Fig. 13). If we use only a row of pixels to compute a mean and standard deviation, we get about the same results as using a square array. But if we use a column of pixels, then we find

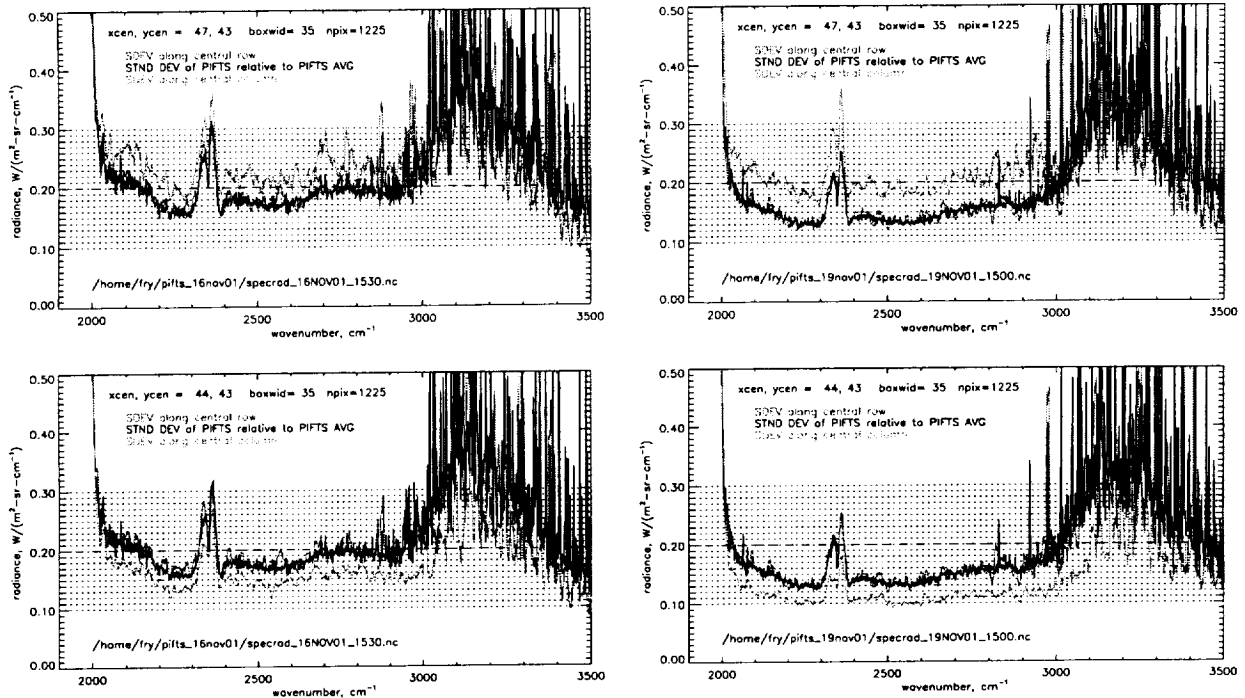


Figure 13: Variation of standard deviations with wavelength and with direction of sampling. The spectral shape in these figures is mainly controlled by responsivity variations. Noise is much reduced on 19 November, but both 19 and 16 November data sets exhibit variability with column value.

a large variation in results depending on column number. In the  $2200\text{--}2300\text{ cm}^{-1}$  region we find values ranging from a low of about  $0.1\text{ ru}$  to a high of  $0.18\text{ ru}$  for the 19 November 15:00 cube, and from a low of about  $0.125\text{ ru}$  to a high of  $0.2\text{ ru}$  for the 15 November 14:55 cube. The variation with column seems to contain a roughly periodic component with a 4-pixel period.

Thus it appears that the PIFTS noise level during the intercomparison tests was substantially higher than during earlier lab tests, and that there are substantial variations in noise level that have spatial patterns suggesting that the readout electronics may itself be excessively noisy. We have so far been unable to determine the cause of the increased and patterned noise levels obtained in recent testing.

### 3.9 Publications.

Some of the results described in previous sections became part of a paper submitted to *Applied Optics* in March 2002 (Sromovsky 2002). The paper is still under review.

## 4 References

- Best, F., H. E. Revercomb, D. LaPorte, R. Knuteson, and W. L. Smith (1997) Accurately Calibrated Airborne and Ground-based Fourier Transform Spectrometers II: HIS and AERI Calibration Techniques, Traceability, and Testing. Presented at the Council for Optical Radiation Measurements (CORM) 1997 Annual Meeting, National Institute of Standards and

Technology (NIST), Gaithersburg, MD. Available from the University of Wisconsin Space Science and Engineering Center, 1225 West Dayton St., Madison WI, 53706.

- Brault, J. W. 1985. Fourier Transform Spectrometry. In *High Resolution in Astronomy*, A. Benz, M. Huber, and M. Mayor, Eds., Geneva Observatory, Sauverny, Switzerland.
- Clough, S. A., J. L. Moncet, R. D. Worsham, M. J. Iacono, and A. Bianco (1991). Radiative transfer development in support of the Atmospheric Radiation Measurement (ARM) Program. *Proceedings of the Second Atmospheric Radiation Measurement (ARM) Science Team Meeting*, pp 21-24. CONF-9110336, U. S. Department of Energy, Washington, D. C.
- Fry, P. M. (2002) PIFTS Data Processing. Internal report available from the Space Science and Engineering Center, 1225 West Dayton St., Madison, WI 53706.
- Revercomb, H.E., L.A. Sromovsky, P.M. Fry, F.A. Best, and D.D. LaPorte (2000) Demonstration of Imaging Fourier Transform Spectrometer (FTS) performance for planetary and geostationary Earth observing. *SPIE 2nd International Asia-Pacific Symposium on Remote Sensing of Atmosphere, Environment, and Space*, 9-12 October 2000, Sendai, Japan.
- Revercomb, H.E., W. L. Smith, R. O. Knuteson, F. A. Best, R. G. Dedecker, T. P. Dirkx, R. A. Herbsleb, G.M. Buchholtz, J. F. Short, and, H.B. Howell (1994) AERI - Atmospheric Emitted Radiance Interferometer. *Eighth Conference on Atmospheric Radiation*. Nashville, TN, 23-28 January, p 180-182.
- Revercomb, H.E., H. Buijs, H.B. Howell, D.D. LaPorte, W.L. Smith, and L.A. Sromovsky (1988) Radiometric Calibration of IR Fourier Transform Spectrometers: Solution to a Problem with the High Resolution Interferometer Sounder. *Applied Optics* **27**, 3210-3218
- Sromovsky, L. A. (2002) Radiometric Errors in Complex Fourier Transform Spectrometry. *Applied Optics*, submitted 29 March 2002.
- Sromovsky, L.A., H.E. Revercomb, and P.M. Fry (2000) Preliminary evaluation of a Planetary Imaging Fourier Transform Spectrometer (PIFTS). *Proceedings of the Fifth Workshop on Infrared Emission Measurements by FTIR*, held on 9-11 February 2000, ABB Bomem, Quebec, Canada.